RESEARCH ARTICLE

WILEY **NMR** IN BIOMEDICINE

Brain investigations of rodent disease models by chemical exchange saturation transfer at 21.1 T

Tangi Roussel[1] | Jens T. Rosenberg[2] | Samuel C. Grant[2,3] (iD) | Lucio Frydman[1,2] (iD)

[1] Department of Chemical and Biological Physics, Weizmann Institute of Science, Rehovot, Israel

[2] National High Magnetic Field Laboratory, Tallahassee, Florida

[3] Department of Chemical & Biomedical Engineering, FAMU-FSU College of Engineering, The Florida State University, Tallahassee, Florida

Correspondence
Lucio Frydman, Department of Chemical and Biological Physics, Weizmann Institute of Science, 76100 Rehovot, Israel.
Email: lucio.frydman@weizmann.ac.il

This study explores opportunities opened up by ultrahigh fields for in vivo saturation transfer brain magnetic resonance imaging experiments. Fast spin-echo images weighted by chemical exchange saturation transfer (CEST) effects were collected on Sprague–Dawley rats at 21.1 T, focusing on two neurological models. One involved a middle cerebral artery occlusion emulating ischemic stroke; the other involved xenografted glioma cells that were followed over the course of several days as they developed into brain tumors. A remarkably strong saturation-derived contrast was observed for the growing tumors when calculating magnetization transfer ratios at *c.* 3.8 ppm. This large contrast originated partially from an increase in the contribution of the amide CEST effect, but mostly from strong decreases in the Overhauser and magnetization transfer contributions to the upfield region, whose differential attenuations could be clearly discerned thanks to the ultrahigh field. The high spectral separation arising at 21.1 T also revealed numerous CEST signals usually overlapping at lower fields. Ischemic lesions were also investigated but, remarkably, magnetization and saturation transfer contrasts were nearly absent when computing transfer asymmetries using either high or low saturation power schemes. These behaviors were consistently observed at 24 hours post-occlusion, regardless of the data processing approach assayed. Considerations related to how various parameters defining these experiments depend on the magnetic field, primarily chemical shifts and T_1 values, are discussed.

KEYWORDS

brain glioma, chemical exchange saturation transfer, ischemic stroke, magnetization transfer, ultrahigh-field MRI

1 | INTRODUCTION

Saturation transfer is a well-known effect in magnetic resonance, which has been exploited in analytical spectroscopic contexts for several decades.[1] This phenomenon has also become widely used in biological settings with the advent of chemical exchange saturation transfer (CEST) and magnetization transfer (MT) measurements. Endogenous contrast mechanisms that arise upon selective irradiation of peaks

associated with either labile hydrogens or other sites, eventually can alter water signal intensity.[1-7] CEST, in particular, highlights molecules carrying labile hydrogens, including fundamental metabolites, such as creatine, glucose, glutamate and urea.[8-11] Chemical exchanges between these species and water can be determined by recording so-called Z-spectra: multi-scan experiments in which the effect on the water peak is monitored upon application of presaturating radiofrequency (RF) pulses irradiating at an array of offsets. Although this frequency-selective saturation procedure forfeits the possibility of interrogating all the labile hydrogens simultaneously, this is compensated by the potential amplification of the site-specific information afforded by CEST. In the slow exchange regime, this amplification will be on the order of $k_{ex}T_1^{water}$, where k_{ex} is the rate of solvent exchange of the labile hydrogen and T_1^{water} is the relaxation time of the solvent.[2,6,7] In favorable cases this magnification can reach approximately 100–1000, leading to the possibility of using CEST as an in vivo metabolic imaging tool. The most prominent CEST peaks do not usually arise from metabolites in either healthy or tumorous brain tissues, but rather from amide groups and aliphatic side-chains in proteins, or from other macromolecular components.[12-14] The reduction in the water signal intensity arising from saturation of endogenous contrast sources positioned 3.5 ppm downfield of water is usually referred to as the amide proton transfer (APT) contribution to CEST magnetic resonance imaging (MRI). Z-spectra also often reveal water saturation on irradiation upfield of the water resonance in a region in which no labile protons resonate. This effect is usually assigned to the saturation of lipid end groups or of protein side-chains, which via direct cross-relaxation with structural water molecules or via cross-relaxation with protons in amides or hydroxyls in exchange with H_2O, result in partial saturation of the bulk water peak. Regardless of the exact transfer pathway, these are known as nuclear Overhauser effect (NOE) contributions.[15,16] Finally, in addition to these relatively narrow dips arising on saturation of specific species, changes in the water signal intensity may arise in vivo when irradiating over a much larger range of frequency offsets – as far as 10 ppm away from the water resonance. These changes originate from the saturation of protons in semi-solid macromolecules, whose dipolar-broadened lines can be subject to couplings in the tens of kilohertz. On irradiation of this homogeneously broadened background, saturation can be transferred to the free water resonance via cross-relaxation or even by direct dipolar coupling with water molecules at a rate k_{MT}; as these free up and become "normal" bulk water molecules, the dominating water signal intensity drops. This forms the basis of the MT contrast, which is often considered as a phenomenon akin to, but distinct from, CEST. In addition to these information-carrying contributions, there may also be contribution to the Z-spectrum associated with changes that the water peak itself experiences when performing off-resonance irradiation. These contributions to the water peak saturation incorporate a variety of relative relaxations (T_1, T_2, T_2^*) and RF (B_1) factors. In order to deal with these "spillover effects", it is customary to compute both CEST- and MT-derived images by performing two experiments in which saturation is symmetrically placed around the water resonance. It is then the relative difference between these two effects, known as the magnetization transfer ratio asymmetry $MTR_{asym}(\Delta\omega)$, which is usually reported in these experiments. Further corrections may have to be introduced to account for shifts in the water resonance position within the targeted region of interest (ROI).[17] To disentangle all of these competing and simultaneous mechanisms that can contribute to MTR_{asym}, an increasing number of sophisticated signal processing approaches have been proposed, including quantitative techniques based on single or multi-Lorentzian fitting models, and on Bloch equation calculations.[16,18-21]

    Z-spectra and images derived from CEST and MT effects depend on physiologically valuable parameters, including metabolic concentrations, temperature and pH.[12,14,22,23] They also depend on parameters that are metabolically less meaningful but spectroscopically important, including the solvent's access to and exchange with the protons of macromolecules and metabolites, as well as the spin relaxation properties of all the species. A particularly important variable in defining the nature of CEST and MT parameters is the magnetic field strength B_0. In addition to the well-known enhancements in sensitivity and resolution arising with increasing B_0, higher fields will separate the frequency differences $\Delta\nu$ (in Hz) between the exchanging species and water. This will, in turn, expand the range of processes that can contribute to the CEST/MT observations, and whose rates k_{ex} and k_{MT} need to be on the order of $\Delta\nu$ (or smaller) in order to enable a substantial magnification of the targeted resonances. In complex systems, such as living tissues, these k values will normally entail a heterogeneous distribution of frequencies; increasing $\Delta\nu$ by moving to higher fields thus increases the range of participating processes, augmenting the experiment's contrast.[21] Furthermore, as the field increases, water, which although a small molecule interacts strongly with its surrounding environment, will lengthen its T_1 with B_0.[24,25] The overall kT_1^{water} product defining MT/CEST's maximum amplification is thus expected to increase with the operating field B_0. Such behavior has been observed in preliminary paramagnetic and diamagnetic CEST measurements,[26,27] and has been reported recently in a preclinical field comparative study,[28] suggesting that the use of ultrahigh fields could open hitherto untapped contrasting possibilities. The present study explores this hypothesis by applying CEST imaging methodologies to examine brain-related conditions on rats at 21.1 T. The two conditions chosen were glioma and stroke, diseases that have been extensively used to study injuries to brain white and gray matter by CEST MRI in the past.[12-15,29-37] In those studies, an MTR_{asym} increase of approximately 2%–10% was observed at c. +3.5 ppm on comparison of glioma with healthy brain tissue.[13,29-32,35,37,38] Moreover, as the chemical exchange rates of amides depend on the tissue microenvironment,[4,14,15] APT-derived CEST weighting has been proposed as an imaging method to quantify pH and, from there, to detect brain strokes.[12] In this study, an intense MTR_{asym} contrast was observed at 21.1 T on rat glioma tissues, considerably larger than that hitherto observed at lower fields. Several processing methods were used to identify and quantify the various contributions to this enhanced MTR_{asym}. By contrast, the changes in MTR_{asym} did not reach statistical significance in the stroke cases, providing much weaker reporters than T_2 or diffusion observables when examined at 24 hours post-occlusion. Potential explanations for these features, and prospects of additional ultrahigh magnetic field studies in these brain investigations, are discussed.

2 | EXPERIMENTAL METHODS

2.1 | Animal handling

All surgical procedures were carried out under aseptic conditions in accordance with the guidelines for animal experimentation from the ethical committee of the Florida State University (FSU) Animal Care and Use Committee. FSU is registered as a research facility with the United States Department of Agriculture (USDA Registration #58-R-0001) and has an Animal Welfare Assurance number (#A3854–01) on file with the US Public Health Service. All animal procedures were undertaken according to these regulatory bodies and AAALAC guidelines, under the direction of a veterinarian who is certified as a specialist in laboratory animal medicine by the American College of Laboratory Animal Medicine (ACLAM). Naïve Sprague–Dawley rats were purchased from Envigo Corp. (Tampa, FL) and delivered 1 week prior to surgery for acclimatization to the new environment. All animals were housed individually in a 12-hour night/12-hour daylight cycle with water and food available *ad libitum*. For each disease model, male Sprague–Dawley rats weighing between 200 and 250 g were randomly chosen from the cohort of available animals. Seven animals were chosen to provide statistically significant results by means of power analysis, whilst, at the same time, minimizing the number of animals used. After an aseptic preparation, the surgical site was infiltrated with 0.2 mL of 0.5% bupivicaine (Hospira, Lake Forest, IL). In addition, 0.05 mg/kg of buprenorphine (Reckitt Benckiser Pharmaceuticals Inc., Richmond, VA) was injected subcutaneously and every 4–6 hours, or as needed, for pain management. After surgery, all animals were given pre-warmed fluids (3–5 mL of 1 × phosphate-buffered saline [PBS]) intraperitoneally to facilitate recovery. Animals were left to recover in a pre-warmed (37°C) recovery cage. Euthanasia was performed in accordance with the 2013 American Veterinary Medical Association (AVMA) Guidelines on Euthanasia. After the last MRI session, animals were anesthetized with isoflurane and exposed to CO_2 for fast and pain-free euthanasia. Once respiratory failure and cardiac arrest had occurred, a cervical dislocation was performed.

2.2 | Ischemic animal model

Seven juvenile male Sprague–Dawley rats were anesthetized with 5% isoflurane (Baxter, Deerfield, IL) in an induction chamber and maintained on 3%–4% isoflurane during the surgical procedure. After administration of a local nerve block (bupivicaine), the common carotid artery, external carotid artery and internal carotid artery were exposed by blunt and sharp dissection. A 3.0-cm filament with a 0.35-mm-thick and 2–3 mm-long rubber coating (Doccol Corp., Redlands, CA) was inserted through the external carotid artery. The filament was guided 1.9 cm into the internal carotid artery or until the middle carotid artery was blocked. The transient occlusion occurred for 1.5 hours, followed by re-anesthetization and removal of the filament. The animals were imaged 24 hours following the occlusion; no mortalities were documented during the course of the experiments.

2.3 | Glioma animal model

9L glioma cells were cultured and expanded in 75-cm³ tissue culture flasks with Dulbecco's modified Eagle's medium (DMEM) (Sigma Chemical Co., St Louis, MO) supplemented with 10% fetal bovine serum (Atlanta Biological, Atlanta, GA), 1% antibiotics/antimyotics (Gibco, Invitrogen Corp., Carlsbad, CA) and 0.1% gentamycin (Invitrogen Corp.). Cells were kept at a temperature of 37°C and under 5% CO_2. Immediately before implantation surgery, cells were harvested with trypsin (Gibco, Invitrogen Corp.), pelleted by centrifugation and re-suspended in PBS. For intra-cranial implantation, 11 Sprague–Dawley rats were used. Animals anesthetized with isoflurane were secured in a stereotaxic frame with a continuous flow of 2%–3% isoflurane. A 1-cm mid-line incision was made over the skull and the dermal tissues were kept separated by bull clamps. Using Bregma as a reference, a 1-mm burr hole was made 2 mm anterior and 2.5 mm lateral. Using a sterile Hamilton syringe (Sigma-Aldrich, St Louis, MO), 100 000 rat 9 L glioma cells in 10 μL of sterile PBS were injected at a depth of 3.5 mm from the skull. Immediately after the removal of the syringe, bone wax was used to seal the burr hole, and 70% ethanol was applied to the skull to prevent any cells from forming exogenous tumors. The incision was then sealed with sutures. Animals were imaged 7 and 11 days following implantation. Two rats died between days 7 and 11.

2.4 | CEST MRI acquisitions

All data were acquired using the 105-mm bore, 21.1-T (900-MHz) vertical magnet available at the National High Magnetic Field Laboratory MRI/MRS user facility in Tallahassee, Florida.[39] The magnet is equipped with a Bruker Avance III console running Paravision® 5.1 (Bruker Biospin, Billerica, MA) and imaging gradients (Resonance Research Inc., Billerica, MA) delivering a peak strength of 600 mT/m with rise times of 120 μs. A custom-built transmit/receive quadrature double-saddle surface coil was used in these ^{1}H magnetic resonance experiments, whose performance, including B_1 specifications, has been described recently.[40] The coil is part of a probe equipped with a bite-bar supplying continuous flow of anesthesia and provisions to maintain animals at a constant temperature. Prior to their in vivo imaging, all animals were anesthetized with 5% isoflurane; this was then lowered to 2% and adjusted to maintain a respiratory rate between 30 and 40 breaths/min as monitored with a pneumatic pillow situated under the animal (SA Instruments Inc., Stony Brook, NY). Scout fast low-angle shot (FLASH, echo time/repetition time [TE/TR] = 4/50 ms) images were collected to help with animal positioning; this was followed by CEST-weighted ^{1}H rapid

acquisition with relaxation enhancement (RARE) spin echo (SE) images, collected with TE/TR = 9/5000 ms. As CEST-based MRI is an intrinsically time-consuming experiment, its ability to generate neurological contrast for the aforementioned models was studied at 21.1 T in two experimental stages. One stage involved a low-resolution, fast protocol; the second was a lengthier protocol with high spatial and spectral resolution plus inhomogeneity corrections, aimed at better defining the possibilities of CEST at this field.

2.4.1 | Fast, low-resolution CEST MRI

Five animals with middle cerebral artery occlusion (MCAO) and six glioma-bearing animals were scanned using a fast, low-resolution CEST MRI protocol. These images were acquired from a 32×32-mm^2 field of view, using a slice thickness of 1 mm and an in-plane resolution of 250×250 μm^2. The CEST preparation module consisted of a train of 400 10-ms Gaussian pulses with a B_1 field of 3.5 μT, each followed by a low-intensity spoiler gradient. To obtain full Z-spectra, the frequency offset of the saturating pulse train was varied between −10 and +10 ppm relative to water, with a 1-ppm increment step between ±10 and ± 4 ppm, and a 0.5-ppm step between −4 and + 4 ppm (23 increments in total). The total scan time for this CEST MRI protocol was c. 30 minutes.

2.4.2 | High-resolution CEST MRI

Two animals with MCAO and five glioma-bearing animals were scanned using a high-spectral-resolution CEST MRI protocol. These images were acquired from a 32×32-mm^2 field of view, using a slice thickness of 1 mm and an in-plane resolution of 200×200 μm^2. The CEST preparation module consisted of a train of 400 10-ms Gaussian pulses with a B_1 field of 1.5 μT, with the frequency offset of these pulses varied between −5 and +5 ppm relative to water in 0.2-ppm steps (56 increments). CEST images were also recorded at ±100, ±20 and ± 10 ppm in order to establish the wider Z-spectral contributions during quantification. Water saturation shift referencing (WASSR) maps[17] were also acquired for these experiments, and their impact on the CEST data when attempting to correct for water frequency shifts was assessed. These WASSR preparation modules consisted of a single 200-ms saturation Gaussian pulse with a B_1 field of 0.5 μT, and frequency offsets varying from −0.3 to +0.3 ppm with a 0.05-ppm step (13 increments). In order to check the field homogeneity and the RF transmission performance, B_0 and B_1 maps were acquired using a three-dimensional phase imaging sequence (Fieldmap, 128×128 matrix) and a saturated double-angle method, respectively.[41] The total scan time for this CEST MRI protocol was c. 3 hours.

2.5 | Data processing

CEST/MT-weighted images were processed and quantified using a customized MATLAB® (The Mathworks Inc, Nantucket, MA) code. This quantification involved computing MTR$_{asym}$ maps, generated as:

$$MTR_{asym}(\Delta\omega) = \frac{S(-\Delta\omega) - S(+\Delta\omega)}{S_0} \times 100$$

where $S(\pm\Delta\omega)$ reflects the water signal intensity on irradiation at two frequencies symmetrically placed with respect to water, and S_0 is a water reference signal acquired when the saturation frequency is far off-resonance (+100 ppm in this study). With MTR$_{asym}$ maps obtained in this manner, the rat brain images were manually segmented, and two ROIs were selected highlighting either normal or diseased (ischemic or glioma) brain tissues. For each animal, the optimal saturation frequency $\Delta\omega$ yielding the highest MTR$_{asym}$ contrast between normal and diseased tissues was estimated and employed for later statistical use. WASSR maps were generated using a spline interpolation and MTR$_{asym}$ maps were calculated with and without B_0 correction. Lorentzian fit difference (LFD) processing[20] was also applied to each voxel in the analysis of their corresponding Z-spectra. The purpose of the LFD was to extract CEST components after suppression of the direct water saturation (spillover) effects, and the procedure was performed in two steps. First, an automatic fitting procedure adjusted the amplitude and damping parameters of a double-Lorentzian model centered on 0 ppm using a least-squares optimization method; subsequently, the residual of this double-Lorentzian fit was extracted to reveal any residual CEST components disturbing the symmetry of a pure water Z-spectrum. Upfield and downfield CEST contributions were also quantified using another method: the so-called three-offset technique.[15,34] Here the Z-spectrum is linearly interpolated between two a priori chosen frequency offsets of interest (for instance, two offsets, 1 ppm apart), and then a search is made for the maximum difference between this fitted line and the original spectrum, so as to reveal the offset and amplitude of any CEST component potentially present. APT/NOE contributions were quantified in these two ways between frequency offsets of +2/+4 ppm and −2/−5 ppm, respectively, and quantitative APT/NOE maps were thus generated. Other spectral contributions centered at +2 and −1.8 ppm were quantified using [+1.6;+2.4] and [−2;−1.5] ppm chemical shift ranges.

2.6 | Statistical analysis

Quantitative measures were averaged over the indicated ROIs and are presented with ±standard deviation of the mean. Statistical significance was determined with Student's t-test with significance set at the P values indicated in the text.

3 | RESULTS

Figure 1 shows representative T_2-weighted, B_1 and WASSR maps obtained on an animal with MCAO at 21.1 T. The quadrature double-saddle surface coil used in these experiments[40] is able to generate a relatively homogeneous B_1 coverage of the rat brain, with only slight drops in power in the lower and peripheral parts. Similarly, B_0 field homogeneity was excellent in the upper and central parts of the brain, as evidenced by the WASSR maps. In general, the largest frequency shifts were evidenced in the lower parts of the brain, probably originating from distortions imposed by proximity to the nose and to the ear canals, compounded by low signal-to-noise ratio (SNR) due to the surface coil sensitivity profile.

Figures 2–4 summarize various features observed when CEST experiments were carried out on glioma-bearing animals. The maps in Figures 2 and 3 illustrate axial RARE results acquired for different Z-spectral offsets, for a glioma-implanted rat at days 7 and 11 post-injection of the cancerous cells and for two different saturation conditions. For all cases, intensification and expansion of the contrast in the right hemisphere
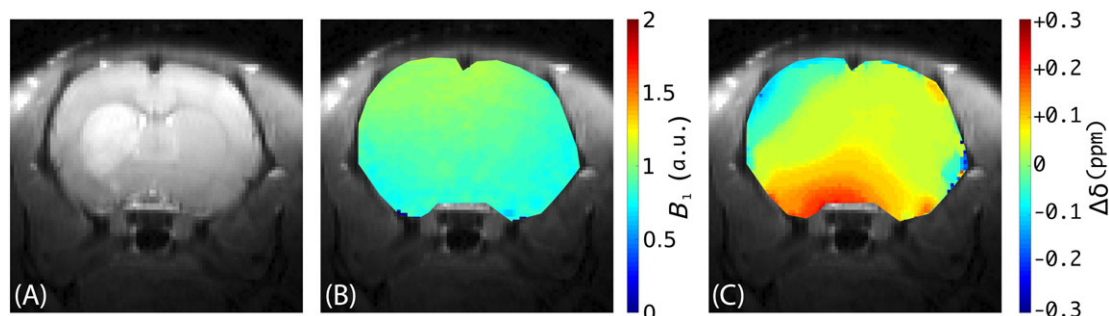

FIGURE 1 Representative T_2-weighted rapid acquisition with relaxation enhancement (RARE) image (A), B_1 map (B) and water saturation shift referencing (WASSR) map (C) acquired in a rat with middle cerebral artery occlusion (MCAO) at 21.1 T. The ischemic tissue is clearly visible in the left hemisphere of the brain on the T_2-weighted image. The B_1 map shows a general homogeneity over the brain with a slight over-tipping effect near the coil (top of the brain), whereas the WASSR map reveals an overall high B_0 homogeneity with ≈0.15 ppm heterogeneities in the lower brain regions
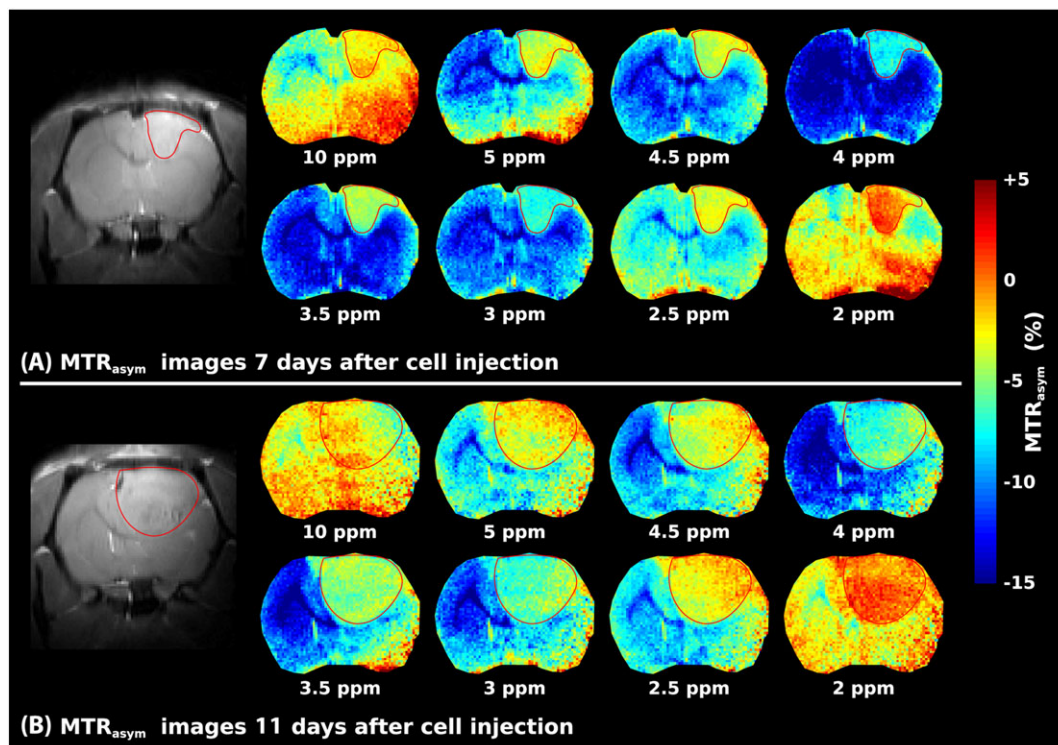

FIGURE 2 Magnetization transfer ratio asymmetry (MTR_{asym}) maps obtained on a glioma-implanted rat brain using the low-power (B_1 = 1.5 μT) high-resolution chemical exchange saturation transfer (CEST) imaging protocol for two different days following cell implantation. A, 7 days after the injection of 9L glioma cells. B, 11 days after the injection of 9L glioma cells. In addition to the dominant tumor-derived features, a relatively strong positive MTR_{asym} can be observed in the lower parts of the brain for some chemical shifts, probably because of low signal-to-noise ratio (SNR) and B_0 inhomogeneities originating from the ear canals and the sinuses (cf. Figure 1). Marked by the red contours are the approximate regions invaded by the glioma
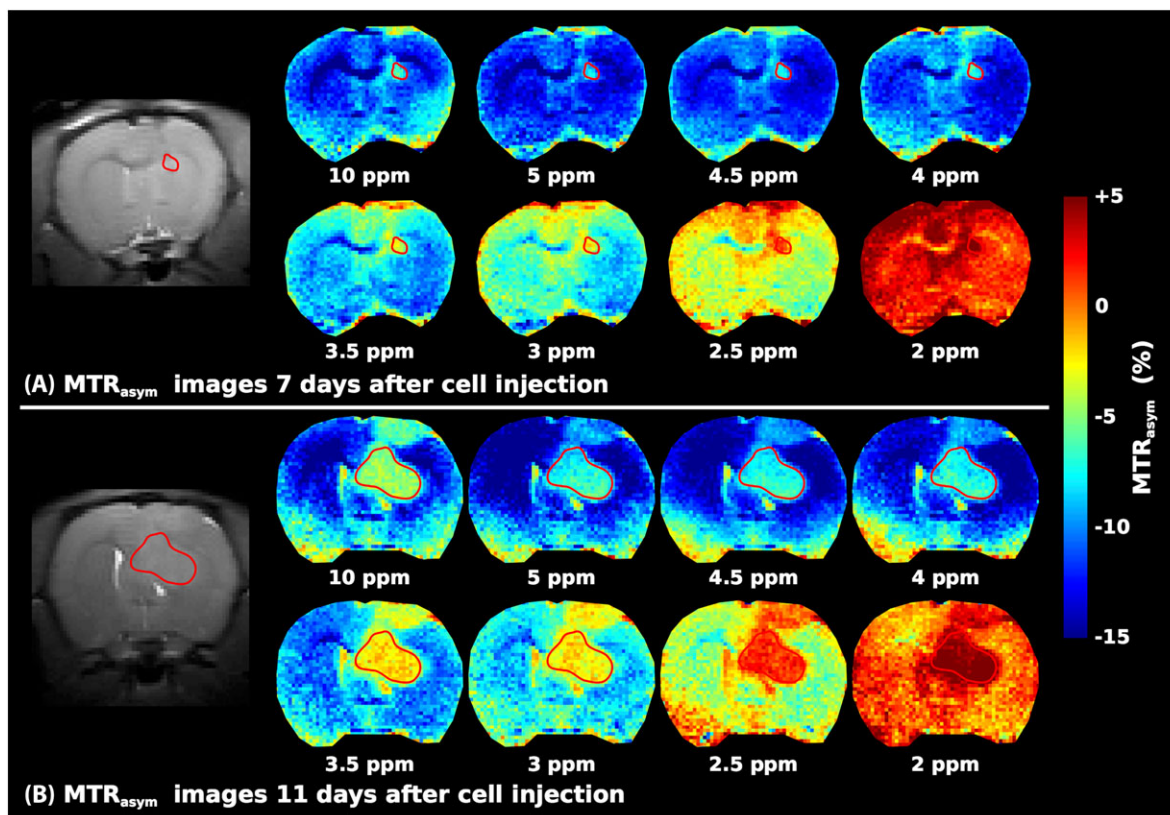
FIGURE 3 Magnetization transfer ratio asymmetry (MTR$_{asym}$) maps obtained on a glioma-implanted rat brain using the low-resolution, high-power chemical exchange saturation transfer (CEST) imaging protocol for two different days following cell implantation. A, 7 days after the injection of 9L glioma cells. B, 11 days after the injection of 9L glioma cells. The radiofrequency (RF) saturation used here was stronger (3.5 μT) than that used in Figure 2, and allowed the observation of an intense glioma contrast from 2.5 to 10 ppm, probably originating from magnetization transfer effects (red encircled regions)
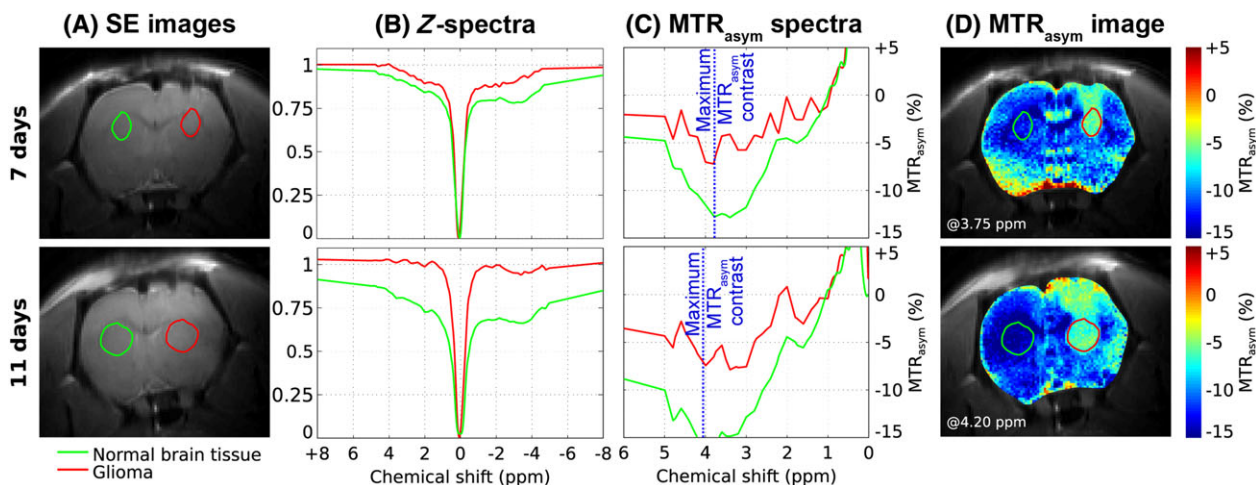

FIGURE 4 Z-spectra and magnetization transfer ratio asymmetry (MTR$_{asym}$) maps obtained on a glioma-implanted rat for two different points in time, under low γB_1 saturating conditions. Top row: results observed 7 days after 9 L glioma cell injection. Bottom row: results observed 11 days after 9L glioma cell injection. A, Anatomical rapid acquisition with relaxation enhancement (RARE) images showing the regions of interest (ROIs) of normal brain and diseased regions. Notice the weak contrast between the two. B, Localized Z-spectra extracted from normal brain (green) and glioma (red) tissues. C, Corresponding MTR$_{asym}$ spectra. D, MTR$_{asym}$ maps extracted at the chemical shift of maximum contrast (indicated in blue in C) for this particular animal

can be seen as the tumor develops. Interestingly, similar contrasts between normal brain and glioma-invaded tissues are observed under low- and high-B_1 CEST conditions. Nevertheless, the low-B_1 experiments allowed the observation of spectrally selective CEST effects by reducing the sensitivity to the broad MT effects otherwise observable up to 10 ppm. Figure 4 offers a description of this, with the MTR$_{asym}$ contrast displayed by

glioma tissue when recorded (on a different animal) using the high-resolution CEST imaging protocol. Shown in Figure 4A are the anatomical T_2-weighted images, which themselves show only a weak contrast stemming from the tumor. Figure 4B shows the Z-spectral data observed as a function of frequency, when integrated over ROIs associated with healthy (green) and diseased (red) tissues. The large differential CEST changes are highlighted by the MTR_{asym} spectrum, as this results from the subtraction of contributions on opposite sides of the water resonance (Figure 4C). The CEST MTR_{asym} maps shown in Figure 4D illustrate how, on choosing the most intense asymmetry offset, the tumor can be clearly distinguished from healthy tissue at both stages (similar maps are presented for additional MTR_{asym} offsets in Figure 2). When considered over the $n = 5$ animal cohort studied under the low-power conditions, the maximum MTR_{asym} contrast for glioma tissue was statistically observed at 4.0 ± 0.5 ppm for the day-7 time point and at 3.7 ± 0.1 ppm for the day-11 time point. For these offsets, the average changes in MTR_{asym} between normal and glioma brain tissue were 6.2% ± 1.9% and 7.3% ± 1.5%, respectively.

Figure 5 shows an alternative way of processing these CEST data. These images show quantitative maps obtained for different irradiation frequencies using the LFD method on data acquired from a rat bearing a 7-day glioma. As a reminder, this Lorentzian deconvolution is performed
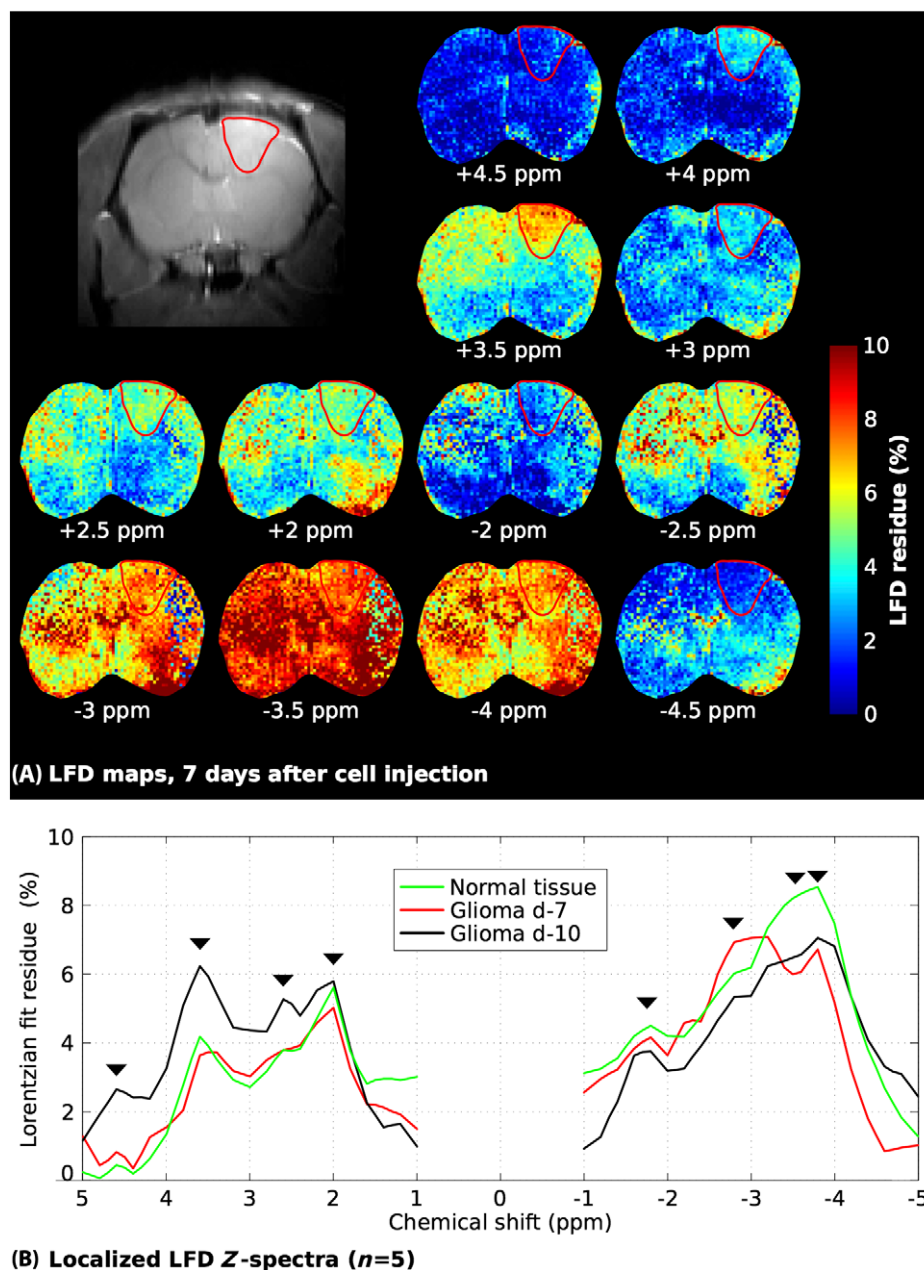

(A) LFD maps, 7 days after cell injection

(B) Localized LFD Z-spectra ($n=5$)

FIGURE 5 Quantitative chemical exchange saturation transfer (CEST) maps obtained for different saturation frequencies using the Lorentzian fit difference (LFD) method. A, LFD maps arising on a rat bearing a day-7 glioma. Note the strong positive contrast appearing at +3.5 ppm (amide proton transfer, APT) and the slight negative contrast observed at −3.5 ppm (nuclear Overhauser effect, NOE) for the tumorous tissue. B, Average Z-spectra obtained using LFD over different tissues and at different stages, over the $n = 5$ animal cohort studied. The black arrows indicate multiple spectral features arising in these water-detected data at c. −3.8 −3.5, −3.0, −1.8, +2.0, +2.6, +3.5 and + 4.6 ppm, and the glioma-induced changes in these contributions as a function of the days elapsed since injection. The vertical scale denotes % with respect to the maximum water signal S_0

to remove the effects of direct water saturation, as well as potentially also MT effects (although the latter are relatively weak under the low-B_1 conditions pertaining to these data); the residual highlights all remaining, physiologically relevant mechanisms acting as the main sources of contrast. A weak contrast is observed on saturation at c. −3.5 ppm in the region normally associated with aliphatic resonances, and a positive contrast appears at +3.5 ppm in the region normally associated with labile hydrogens and APT effects. This is opposite to the trend shown by the localized Z-spectra illustrated in Figure 4, which revealed a strong decrease in the absolute value of the MTR$_{asym}$ contrast for cancerous tissues. Figure 5B provides a different rendering of these changes and illustrates, after averaging over normal and diseased brain ROIs for the full animal cohort studied at B_1 = 1.5 µT, the Z-spectra arising for different chemical shifts after subtraction of the water/MT spillover contributions. These LFD results highlight the APT increase associated with the glioma. The signal processing approach, in combination with the high-resolution Z-spectrum acquisition conditions, shows a number of finer Z-spectral features at this 21.1-T field. These include downfield CEST contributions usually ascribed mostly to intrinsic protein constituents: amides at +3.5 ppm, side-chain amines at +2.5 ppm,[42] creatine plus other amines usually assigned to the +2-ppm peak (although this has also been tentatively connected by magic angle spinning nuclear magnetic resonance cross-relaxation experiments to aromatic sidechains[43]) and a novel feature arising at +4.6 ppm. The spectral LFD deconvolution of the upfield NOE hump also reveals a fine structure, including a − 1.8-ppm NOE-mediated peak that has been associated with choline head groups[44] and peaks at −3.0, −3.5 and − 3.8 ppm that have been related to macromolecular methylene and methyl protons.[45]

Figure 6 shows a further evaluation of these results for the n = 5 animal cohort in the low-power glioma study, this time quantifying the CEST behavior based on the "three-offsets" technique reported by Xu et al.[34] This approach also successfully identifies the eight peaks noted in Figure 5; of all these, Figure 6 focuses solely on the four peaks in which potentially significant changes were identified from ROIs containing healthy and glioma-bearing tissues. This quantification evidenced a positive change in intensity when considering the APT region between normal brain and day-11 glioma tissue (Figure 6A, P < 0.1). More significant NOE changes were evidenced by the upfield part of the spectrum (Figure 6B), with a 1.3% decrease (P < 0.05) between normal brain and day-7 glioma tissue, and a 1.4% decrease (P < 0.05) in the case of day-11 glioma tissues. The amine component at +2 ppm and the minor NOE component at −1.8 ppm also showed significant changes (P < 0.1) between normal brain and day-11 glioma tissue (Figure 6C, D).
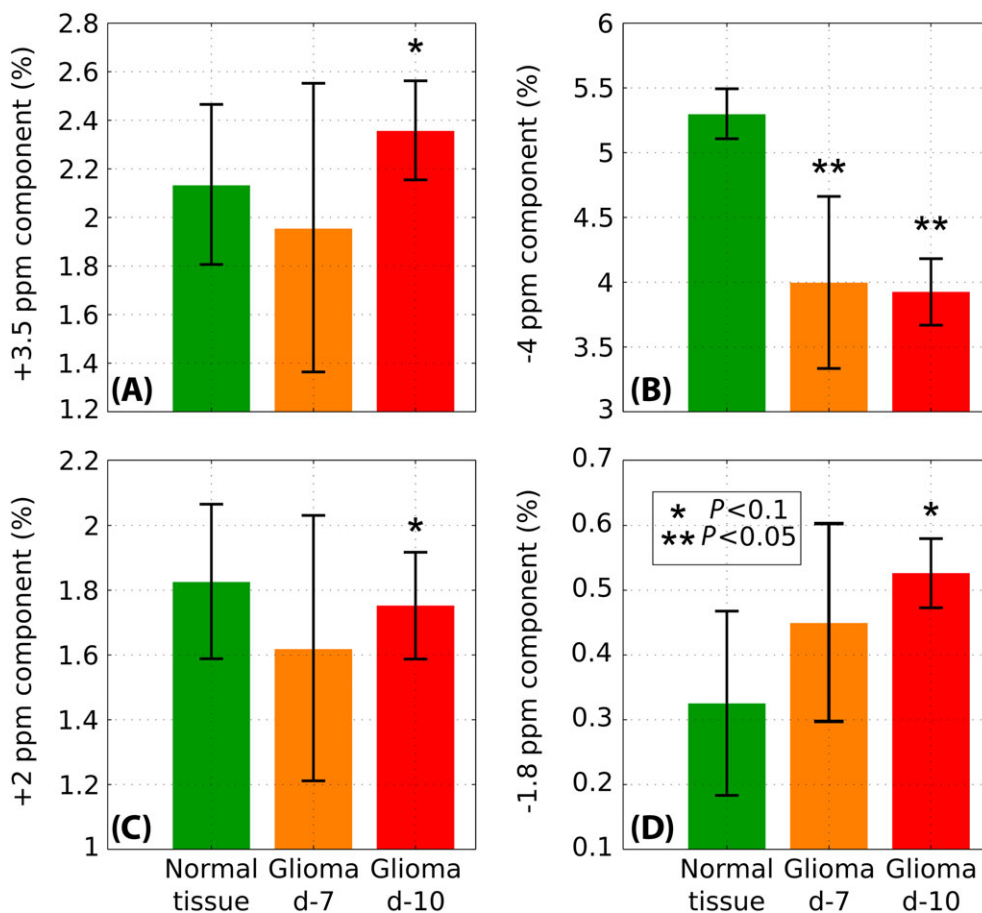

FIGURE 6 Average quantification of the chemical exchange saturation transfer (CEST) contrast changes obtained using the three-offset integration technique for the amide peak at +3.5 ppm (A), the nuclear Overhauser effect (NOE) peak at −4 ppm (B), the amine peak at +2 ppm (C) and the peak at −1.8 ppm (D). The results reflect an n = 5 animal cohort. Vertical axis scales are as in Figure 5B. Statistical significance was determined based on a paired Student's t-test. The error bars represent the standard error of the mean (SEM) obtained over the five animals included in the group study. Green bars represent data from a normal tissue ROI while orange and red bars represent data from glioma ROIs at day 7 and 10, respectively

It is interesting to contrast these glioma data, which are mutually consistent regardless of the adopted data processing approach, with the 21.1-T results observed when the pathology is associated with a MCAO-derived ischemia. Figure 7 shows how this event, clearly seen in the anatomical images of the stroked animals when investigated 24 hours after the injury, fails to reveal a particular chemical shift for which a significant MTR_{asym} is evidenced under the low-power, high-resolution CEST conditions used in the glioma studies. This is further illustrated by the Z-spectral images shown in Figure 8, where the dominant direct water saturation was subtracted using the LFD method. Some contrast features are evident from these residuals, but these do not correspond to the stroke regions. This absence does not mean that the Z-spectra are identical for healthy and stroke regions: in general we observe, under these conditions, a slight decrease in a spectrally broad region in the latter (e.g. Figure 7). This could reflect different MT behaviors, but also differences in the water relaxation characteristics (and thereby in the
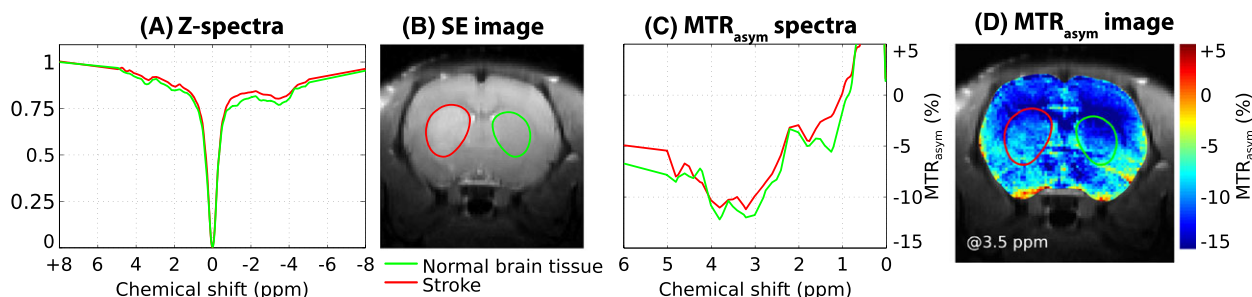

FIGURE 7 Representative chemical exchange saturation transfer (CEST) results obtained in a rat with middle cerebral artery occlusion (MCAO) using the high-resolution CEST imaging protocol. A, Localized Z-spectra extracted from normal brain (green) and ischemic (red) brain tissue regions of interest (ROIs). B, Anatomical rapid acquisition with relaxation enhancement (RARE) image illustrating the targeted ROIs. SE, spin echo. C, Corresponding magnetization transfer ratio asymmetry (MTR_{asym}) spectra for the two ROIs. D, MTR_{asym} map extracted for the whole organ at +3.5 ppm, i.e. close to the offset of highest MTR_{asym} for both stroke and normal regions
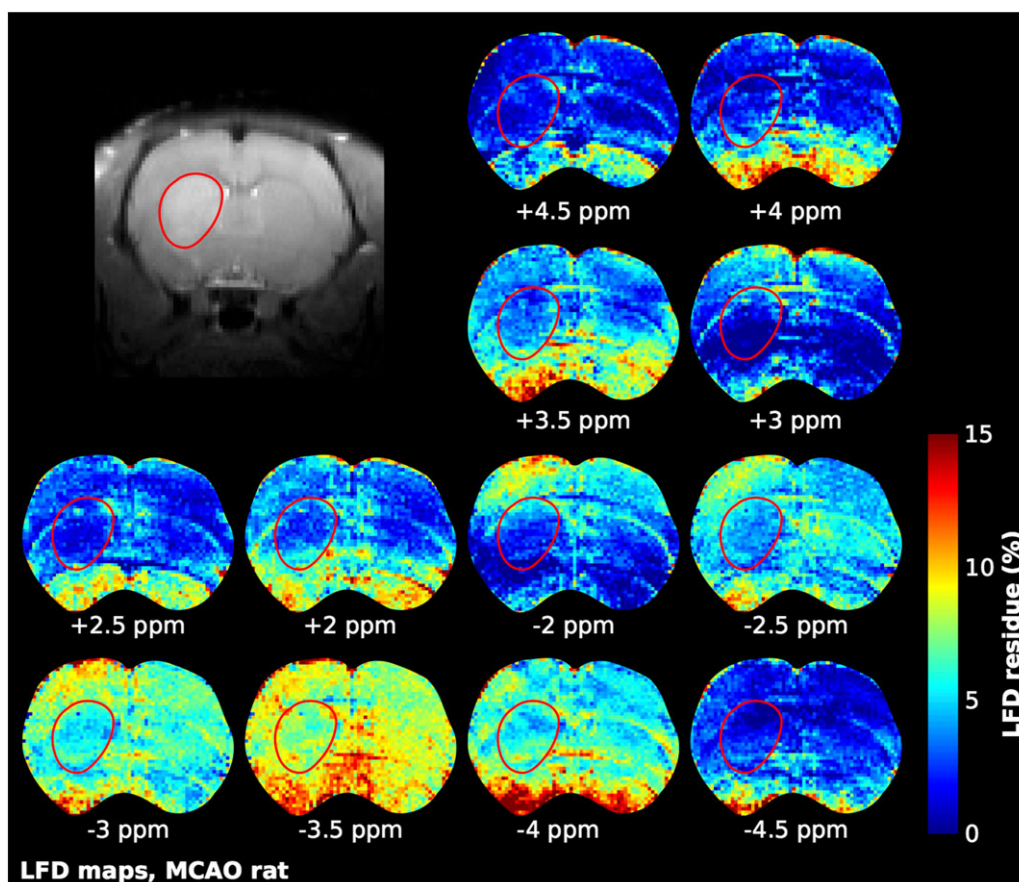

FIGURE 8 Quantitative chemical exchange saturation transfer (CEST) maps obtained for different saturation frequencies using the Lorentzian fit difference (LFD) method on data acquired using the high-resolution CEST imaging protocol on a rat with middle cerebral artery occlusion (MCAO). No specific contrast could highlight the ischemic brain tissue, whose region is illustrated by the red line defining the region of interest (ROI)

spillover and saturation transfer effects) between healthy and diseased tissues. Moreover, unlike in the glioma case, the asymmetry of these saturation transfer plots about the water peak is not significantly distorted on going from one kind of tissue to the other. As illustrated in Supporting Information, a similar behavior is observed when examining animals with MCAO at 24 hours post-occlusion under high-power (B_1 = 3.5 μT) saturating conditions. This robs the 21.1-T MTR_{asym} plots of contrast capabilities: over the n = 5 cohort analyzed using the low-resolution/high-B_1 CEST imaging protocol and the n = 2 cohort analyzed at high-resolution/low B_1, no significant change (P > 0.5) in either APT or NOE regions could be quantified for the ischemic tissues.

4 | DISCUSSION AND CONCLUSIONS

Multiple physical factors suggest that saturation-based contrasts in MRI should benefit from operation at the highest possible fields. The range of chemical exchange rates accessible in this manner would increase because of a larger chemical shift dispersion, expanding, in turn, the nuclear magnetic resonance timescales, whereas water's lengthening in vivo T_1 value[24,25,46] would mean that the imprint of the saturation on the bulk water pool could also be increased.[19,21,42,47] The relation between B_0 strength and CEST, however, is not straightforward. As mentioned, larger CEST effects have been observed for glucose and other agents at 21.1 T than at lower fields.[26,27] NOE and MT effects have also been reported to increase for human gliomas with increasing field.[37] The present 21.1-T study is in agreement with this latter trend as, for both healthy and glioma tissues, enhancements are observable. Subtler, however, is the extraction of systematic conclusions about how these saturation processes depend on the field. Thus, although remarkable MTR_{asym} contrasts were observed at either high or low presaturation powers for glioma, MTR_{asym} effects were always ambiguous for ischemia – a lesion which, at this field and time point following occlusion, could be much more robustly detected with standard T_2-weighted images or by diffusion measurements.[48]

The strong contrast observed at 21.1 T when comparing tumor versus normal brain tissue can be traced to an increase in the downfield chemical exchange effects and to a decrease in the upfield NOE and MT effects. APT increases in brain tumors have been reported at lower fields in animals (4.7 and 9.4 T[13,29,34,35]) and in humans (3 and 7 T[30,37,38]), with the enhancements ranging between +1% and +4%. Interestingly, we were unable to compute a significant correlation between the APT contrasts reported in the literature and the B_0 fields employed. This is not entirely unexpected as, apart from similar MTR_{asym} values, the reported APT contrasts present in the literature are very heterogeneous and were obtained with different acquisition protocols and APT quantification approaches, thus preventing rigurous quantitative comparisons. Nevertheless, and in agreement with literature trends, a significant (P < 0.1) +0.2% APT increase was observed when comparing normal brain to day-11 glioma tissues. The changes in the upfield saturation have been less clearly established for glioma tissue, and only at high preclinical (9.4 T) or clinical (7 T) fields have decreases in CEST effects, ranging between −1% and −2%, been reported for this NOE component, depending on the quantification tool.[31,32,34,37,38,49] In agreement with these reports, a −1.3% to −1.4% decrease was observed in the extent of the upfield saturation peak at 21.1 T; this, together with the increase in APT CEST, contributed to an MTR_{asym} contrast amounting to c. −6.2% when focusing at c. +4.0 ppm under lower power saturation conditions (Figure 4C). An even larger, ≥|5%| drop was observed in the upfield saturation when operating under high-power conditions, which, together with the APT increase, leads to an MTR_{asym} contrast amounting to approximately −15% when focusing at c. +3.3 ppm (Figure 3). This is, to our knowledge, the largest contrast hitherto observed by CEST on gliomas. The sizable drop in MT under these conditions is observable at chemical shifts far away from water – as distant as −10 ppm. Recent studies have suggested that the rise in APT in glioma tissue may be related to an increased protein content in tumors,[50] a claim that remains to be backed by biochemical measurements of total protein contents in normal and malignant brains.[34] Alternatively, the rise in APT could reflect a change in intracellular pH that increases the rate of proton exchange, or the onset of protein unfolding facilitating amide exchanges with water.[14,51] As for the drop observed in the upfield NOE response, this could also be related to structural changes, including protein unfolding or progressive cellular membrane fracture.[16] In any case, of all the effects, it is the drop in MT that yields the main source of contrast between healthy and glioma tissues – an effect that, although to very different extents, occurs regardless of whether a low or high B_1 saturation power is used (see Supporting Information for examples of the latter). MT originates from "immobile" protons present in proteins, macromolecules or lipids, and exhibits a maximum effect c. 2 ppm upfield from the H_2O resonance.[7,52] The MT drop observed in the high-B_1, 21.1-T experiments is in agreement with recent results observed in 9L rat glioma tissue at 9.4 T,[34] even though the increased frequency separation and longer water T_1 of the field used here probably enhances this difference. Although such broad CEST signals strongly compromise the asymmetry analysis when attempting to estimate APT and NOE contributions, the LFD and the three-offsets quantification methods are not sensitive to this effect and provide reliable high-field observables that can highlight the progress of the disease. The exact reasons behind this MT reduction remain to be defined, but it would be reasonable to link them to a degradation of the structural tissue integrity, to an onset of necrosis and to an increase in water content as the glioma grows.[53]

The presence and changes in the dominant MT contribution compromise the estimation of the finer APT and NOE contributions, particularly when attempting an MTR_{asym} analysis at high B_1 saturation. The deconvolution performed by the LFD and three-offsets quantification methods, however, provides reliable observables that can disentangle CEST peaks under moderate B_1 conditions. The use of a high Z-spectral resolution, coupled with the spectral separation power arising at 21.1 T, reveal in this manner APT and NOE contributions at −3.8, −3.0, −1.8, +2.0, +2.6, +3.5 and +4.6 ppm away from the water peak. The two upfield components at −3.8 and −3.0 ppm are usually associated with protein and/or membrane methyl and methylenes, and do not show significant variations between healthy and diseased tissues. Zhang et al.[44] reported a

NOE-mediated signal around −1.6 ppm in acute ischemic rats at 9.4 T, which we believe corresponds to the −1.8 ppm peak observed here. This peak was tentatively assigned to choline phospholipids. Although Zhang et al.[44] saw a minor decrease in this peak in their acute stroke study, the 21.1-T Z-spectra reveal an increase in day-11 glioma compared with normal brain tissues for this peak (Figure 6D). By contrast, no statistically significant change is observed for this peak in rats with more chronic MCAO (Figures 7 and 8). The labile amine sites of creatine and protein guanidino amine groups at c. +2 ppm[54,55] show a slight but significant drop in glioma cases (Figure 6C), in agreement with the literature reporting a decrease in 9 L tumors in rats.[56] A slight increase is observed in tumorous tissues for the +3.5-ppm peak (Figure 6C), which could reflect the onset of protein unfolding and concurrent solvent exposure for the amide peaks. This is also as previously observed at lower fields.[56] Finally, a low-intensity but significantly glioma-increased CEST signal is detected at +4.6 ppm relative to water. To our knowledge, no reports of endogenous CEST agents for such chemical shifts are available; a potential source for this peak could be nicotinamide, which has chemical shifts ranging between 8.6 and 9.6 ppm. Although NAD^+ concentrations in brain are extremely low (≈500 µmol/L), de Graaf and Behar[57] were able to detect this metabolite in vivo using a non-water-suppressed magnetic resonance spectroscopy sequence thanks to its substantial exchange with the solvent.

By contrast with these marked healthy versus tumor tissue effects, saturation transfer imaging at 21.1 T provided poor contrast when applied to the ischemic rat model (Figures 7 and 8). Previous CEST imaging studies have suggested a decrease in APT of +1% to +3% in ischemic brain tissue,[12,14,15,36,44] perhaps reflecting the acidic environment induced by acute ischemia. However, NOE has been reported to remain nearly unchanged by ischemia.[44] The present study revealed differences between ischemic and normal Z-spectra, but no statistically significant MTR_{asym} of LFD peaks emerging at 21.1 T. Indeed, most of the visual differences arising in Figure 7 between normal and ischemic tissues were erased in the images shown in Figure 8 after deconvolution of the direct and MT saturation components. Interestingly, a slight narrowing of the Z-spectra acquired in ischemic tissues can be observed; this could originate from a number of factors, including changes in the relaxation properties of water (as visible on the T_2-weighted images) or from more complex mechanisms involving a pH modulation of both APT and NOE effects.[58] All of our measurements were performed once, at 24 hours post-MCAO; as ischemia is supposed to exhibit a fast temporal evolution, it remains to be seen whether these CEST measurements and their lack of contrast at 21.1 T would vary with time.[36] Regardless of this, these stroke measurements suggest that the more favorable chemical shift dispersion and longer water T_1 characteristically provided by ultrahigh field operation do not always translate into unambiguously stronger CEST peaks.

In summary, CEST methods were applied at 21.1 T to investigate the contrasts arising for two widely investigated neurological disorders. Both of these have been investigated previously in human and rodent models at lower fields; when repeated at ultrahigh fields at low and high B_1 saturation fields, strong endogenous saturation transfer contrasts resulted for MRI of gliomas. The origins of these could be traced to changes in the APT and NOE contributions to CEST, as well as to MT effects originating from the solid-like tissue matrices. Interestingly, the use of ultrahigh field, in combination with relatively low powers and with high-resolution Z-spectral conditions, successfully resolved, in both healthy and glioma brain regions, multiple CEST signals usually entangled at lower fields. New, potentially useful endogenous markers for glioma were also identified in this manner. By contrast, poor MTR_{asym} changes could be observed for ischemic tissues under similar conditions, a limitation whose exact origin is still under examination.

CONFLICTS OF INTEREST

The authors have no conflicts of interest to declare.

ORCID

Samuel C. Grant http://orcid.org/0000-0001-7738-168X
Lucio Frydman http://orcid.org/0000-0001-8208-3521

REFERENCES

1. Wolff SD, Balaban RS. Magnetization transfer contrast (MTC) and tissue water proton relaxation in vivo. *Magn Reson Med.* 1989;10:135-144.

2. Lemaire L, Franconi F, Saint-Andre JP, Roullin VG, Jallet P, Le Jeune JJ. High-field quantitative transverse relaxation time, magnetization transfer and apparent water diffusion in experimental rat brain tumour. *NMR Biomed.* 2000;13:116-123.

3. Ward KM, Aletras AH, Balaban RS. A new class of contrast agents for MRI based on proton chemical exchange dependent saturation transfer (CEST). *J Magn Reson.* 2000;143:79-87.

4. Ward KM, Balaban RS. Determination of pH using water protons and chemical exchange dependent saturation transfer (CEST). *Magn Reson Med*. 2000;44:799-802.

5. Vinogradov E, Sherry AD, Lenkinski RE. CEST: from basic principles to applications, challenges and opportunities. *J Magn Reson*. 2013;229:155-172.

6. Zaiss M, Bachert P. Chemical exchange saturation transfer (CEST) and MR Z-spectroscopy in vivo: a review of theoretical approaches and methods. *Phys Med Biol*. 2013;58:R221-R269.

7. McMahon MT, Gilad AA, Bulte JW, van Zijl PC. *Chemical Exchange Saturation Transfer Imaging: Advances and Applications*. Pan Stanford: Singapore; 2017.

8. Dagher AP, Aletras A, Choyke P, Balaban RS. Imaging of urea using chemical exchange-dependent saturation transfer at 1.5T. *J Magn Res Imaging*. 2000;12:745-748.

9. Cai K, Haris M, Singh A, et al. Magnetic resonance imaging of glutamate. *Nat Med*. 2012;18:302-306.

10. Walker-Samuel S, Ramasawmy R, Torrealdea F, et al. In vivo imaging of glucose uptake and metabolism in tumors. *Nat Med*. 2013;19:1067-1072.

11. Haris M, Singh A, Cai K, et al. A technique for in vivo mapping of myocardial creatine kinase metabolism. *Nat Med*. 2014;20:209-214.

12. McVicar N, Li AX, Gonçalves DF, et al. Quantitative tissue pH measurement during cerebral ischemia using amine and amide concentration-independent detection (AACID) with MRI. *J Cereb Blood Flow Metab*. 2014;34:690-698.

13. Zhou J, Lal B, Wilson DA, Laterra J, van Zijl PCM. Amide proton transfer (APT) contrast for imaging of brain tumors. *Magn Reson Med*. 2003;50:1120-1126.

14. Zhou J, Payen J-F, Wilson DA, Traystman RJ, van Zijl PCM. Using the amide proton signals of intracellular proteins and peptides to detect pH effects in MRI. *Nat Med*. 2003;9:1085-1090.

15. Jin T, Wang P, Zong X, Kim S-G. MR imaging of the amide-proton transfer effect and the pH-insensitive nuclear Overhauser effect at 9.4 T. *Magn Reson Med*. 2013;69:760-770.

16. Lu J, Zhou J, Cai C, Cai S, Chen Z. Observation of true and pseudo NOE signals using CEST-MRI and CEST-MRS sequences with and without lipid suppression. *Magn Reson Med*. 2015;73:1615-1622.

17. Kim M, Gillen J, Landman BA, Zhou J, van Zijl PCM. Water saturation shift referencing (WASSR) for chemical exchange saturation transfer (CEST) experiments. *Magn Reson Med*. 2009;61:1441-1450.

18. Liu D, Zhou J, Xue R, Zuo Z, An J, Wang DJJ. Quantitative characterization of nuclear Overhauser enhancement and amide proton transfer effects in the human brain at 7 Tesla. *Magn Reson Med*. 2013;70:1070-1081.

19. McMahon MT, Gilad AA, Zhou J, Sun PZ, Bulte JWM, van Zijl PCM. Quantifying exchange rates in chemical exchange saturation transfer agents using the saturation time and saturation power dependencies of the magnetization transfer effect on the magnetic resonance imaging signal (QUEST and QUESP): pH calibration for poly-L-lysine and a starburst dendrimer. *Magn Reson Med*. 2006;55:836-847.

20. Zaiss M, Schmitt B, Bachert P. Quantitative separation of CEST effect from magnetization transfer and spillover effects by Lorentzian-line-fit analysis of z-spectra. *J Magn Reson*. 2011;211:149-155.

21. van Zijl PCM, Yadav NN. Chemical exchange saturation transfer (CEST): what is in a name and what isn't? *Magn Reson Med*. 2011;65:927-948.

22. Delli Castelli D, Ferrauto G, Cutrin JC, Terreno E, Aime S. In vivo maps of extracellular pH in murine melanoma by CEST-MRI. *Magn Reson Med*. 2014;71:326-332.

23. Longo DL, Bartoli A, Consolino L, et al. In vivo imaging of tumor metabolism and acidosis by combining PET and MRI-CEST pH imaging. *Cancer Res*. 2016;76:6463-6470.

24. Rooney WD, Johnson G, Li X, et al. Magnetic field and tissue dependencies of human brain longitudinal ^1H_2O relaxation in vivo. *Magn Reson Med*. 2007;57:308-318.

25. Shemesh N, Rosenberg JT, Dumez J-N, Grant SC, Frydman L. Metabolic T1 dynamics and longitudinal relaxation enhancement in vivo at ultrahigh magnetic fields on ischemia. *J Cereb Blood Flow Metab*. 2014;34:1810-1817.

26. Cornnell HH, Grant SC, Rosenberg JT, et al. Characterization of paramagnetic lanthanide ion complexes as MRI contrast agents as a function of magnetic field strength. In: *15th Joint Annual International Society for Magnetic Resonance in Medicine Conference*, Berlin, Germany, 2007; 861.

27. Markovic S, Rosenberg J, Helsper S, et al. Maternal and fetal glucose uptake followed by chemical exchange saturation transfer imaging (glucoCEST) on pregnant mice at 21.1 T. In: *25th Joint Annual International Society for Magnetic Resonance in Medicine Conference*, Honolulu, HI, USA, 2017; 1031.

28. Chung JJ, Choi W, Jin T, Lee JH, Kim S-G. Chemical-exchange-sensitive MRI of amide, amine and NOE at 9.4 T versus 15.2 T. *NMR Biomed* 2017;30:e3740.

29. Salhotra A, Lal B, Laterra J, Sun PZ, van Zijl PCM, Zhou J. Amide proton transfer imaging of 9L gliosarcoma and human glioblastoma xenografts. *NMR Biomed*. 2008;21:489-497.

30. Zhou J, Blakeley JO, Hua J, et al. Practical data acquisition method for human brain tumor amide proton transfer (APT) imaging. *Magn Reson Med*. 2008;60:842-849.

31. Jones CK, Huang A, Xu J, et al. Nuclear Overhauser enhancement (NOE) imaging in the human brain at 7T. *Neuroimage*. 2013;77:114-124.

32. Zaiss M, Kunz P, Goerke S, Radbruch A, Bachert P. MR imaging of protein folding in vitro employing nuclear-Overhauser-mediated saturation transfer. *NMR Biomed*. 2013;26:1815-1822.

33. Sagiyama K, Mashimo T, Togao O, et al. In vivo chemical exchange saturation transfer imaging allows early detection of a therapeutic response in glioblastoma. *Proc Natl Acad Sci U S A*. 2014;111:4542-4547.

34. Xu J, Zaiss M, Zu Z, et al. On the origins of chemical exchange saturation transfer (CEST) contrast in tumors at 9.4 T. *NMR Biomed*. 2014;27:406-416.

35. Heo H-Y, Zhang Y, Lee D-H, Hong X, Zhou J. Quantitative assessment of amide proton transfer (APT) and nuclear Overhauser enhancement (NOE) imaging with extrapolated semi-solid magnetization transfer reference (EMR) signals: application to a rat glioma model at 4.7 Tesla. *Magn Reson Med* 2015;75:137-149.

36. Li H, Zu Z, Zaiss M, et al. Imaging of amide proton transfer and nuclear Overhauser enhancement in ischemic stroke with corrections for competing effects. *NMR Biomed*. 2015;28:200-209.

37. Zaiss M, Windschuh J, Goerke S, et al. Downfield-NOE-suppressed amide-CEST-MRI at 7 Tesla provides a unique contrast in human glioblastoma. *Magn Reson Med* 2016;77:196-208.

38. Zaiss M, Windschuh J, Paech D, et al. Relaxation-compensated CEST-MRI of the human brain at 7T: unbiased insight into NOE and amide signal changes in human glioblastoma. *Neuroimage*. 2015;112:180-188.

39. Markiewicz WD, Brey WW, Cross TA, et al. A decade of experience with the ultrawide-bore 900-MHz NMR magnet. *IEEE J Adv Supercon*. 2015;25:1-5.

40. Rosenberg JT, Shemesh N, Muniz JA, Dumez J-N, Frydman L, Grant SC. Transverse relaxation of selectively excited metabolites in stroke at 21.1 T. *Magn Reson Med*. 2017;77:520-528.

41. Cunningham CH, Pauly JM, Nayak KS. Saturated double-angle method for rapid B_1^+ mapping. *Magn Reson Med*. 2006;55:1326-1333.

42. Desmond KL, Moosvi F, Stanisz GJ. Mapping of amide, amine, and aliphatic peaks in the CEST spectra of murine xenografts at 7 T. *Magn Reson Med*. 2014;71:1841-1853.

43. Chen J-H, Sambol EB, Decarolis P, et al. High-resolution MAS NMR spectroscopy detection of the spin magnetization exchange by cross-relaxation and chemical exchange in intact cell lines and human tissue specimens. *Magn Res Med*. 2006;55:1246-1256.

44. Zhang X-Y, Wang F, Afzal A, et al. A new NOE-mediated MT signal at around −1.6ppm for detecting ischemic stroke in rat brain. *Magn Reson Imaging*. 2016;34:1100-1106.

45. Behar KL, Ogino T. Characterization of macromolecule resonances in the ^{1}H NMR spectrum of rat brain. *Magn Reson Med*. 1993;30:38-44.

46. Dobre MC, Uğurbil K, Marjanska M. Determination of blood longitudinal relaxation time (T1) at high magnetic field strengths. *Magn Reson Imaging*. 2007;25:733-735.

47. Henkelman RM, Stanisz GJ, Graham SJ. Magnetization transfer in MRI: a review. *NMR Biomed*. 2001;14:57-64.

48. Leftin A, Rosenberg JT, Solomon E, Bejarano FC, Grant SC, Frydman L. Ultrafast in vivo diffusion imaging of stroke at 21.1 T by spatiotemporal encoding. *Magn Reson Med*. 2015;73:1483-1489.

49. Paech D, Burth S, Windschuh J, et al. Nuclear Overhauser enhancement imaging of glioblastoma at 7 Tesla: region specific correlation with apparent diffusion coefficient and histology. *PLoS One*. 2015;10:e0121220.

50. Yan K, Fu Z, Yang C, et al. Assessing amide proton transfer (APT) MRI contrast origins in 9 L gliosarcoma in the rat brain using proteomic analysis. *Mol Imaging Biol*. 2015;17:479-487.

51. Wen Z, Hu S, Huang F, et al. MR imaging of high-grade brain tumors using endogenous protein and peptide-based contrast. *Neuroimage*. 2010;51:616-622.

52. Swanson S, Pang Y. MT is symmetric but shifted with respect to water. In: *11th Annual International Society for Magnetic Resonance in Medicine Conference*, Toronto, ON, Canada, 2003; 660.

53. Upadhyay N, Waldman AD. Conventional MRI evaluation of gliomas. *Br J Radiol*. 2011;84 (Spec No 2):S107-S111.

54. Zhang XY, Xie J, Wang F, et al. Assignment of the molecular origins of CEST signals at 2 ppm in rat brain. *Magn Reson Med*. 2017;78:881-887.

55. Chen L, Zeng H, Xu X, et al. Investigation of the contribution of total creatine to the CEST Z-spectrum of brain using a knockout mouse model. *NMR Biomed*. 2017;30:e3834.

56. Cai K, Singh A, Poptani H, et al. CEST signal at 2ppm (CEST@2ppm) from Z-spectral fitting correlates with creatine distribution in brain tumor. *NMR Biomed* 2014;28:1-8.

57. de Graaf RA, Behar KL. Detection of cerebral NAD(+) by in vivo ^{1}H NMR spectroscopy. *NMR Biomed*. 2014;27:802-809.

58. Heo HY, Zhang Y, Burton TM, et al. Improving the detection sensitivity of pH-weighted amide proton transfer MRI in acute stroke patients using extrapolated semisolid magnetization transfer reference signals. *Magn Reson Med*. 2017;78:871-880.

SUPPORTING INFORMATION

Additional supporting information may be found online in the Supporting Information section at the end of the article.